Chapter 15

Geophysical ERT

Alistair Boyle, Paul Wilkinson

15.1 Introduction

In geophysics, electrical measurement techniques to estimate near-surface impedances were initially developed in the context of mineral prospecting by Conrad Schlumberger in 1911 [1, 2] and have been widely used in subsurface investigations ever since. Geoelectric imaging is used world-wide in industry, consultancy and academia, and is the subject of considerable ongoing research and development. Terminology in geophysics has evolved and what was initially referred to as "vertical electrical sounding" (a one-dimensional layered Earth problem) has been refined to Electrical Resistivity Tomography (ERT). Electrical Resistivity Imaging (ERI) is also used in some literature as an alternative to the use of ERT. Resistivity (units: Ωm), the reciprocal of conductivity (units: S/m), is generally the preferred unit when discussing geological phenomena.

It is important to recognize that, mathematically, biomedical EIT and geophysical ERT solve the same equations; the Calderón Problem. Nonetheless, there are some important distinctions in geophysics for specific applications. In particular, ERT is usually performed at much lower frequencies (1 Hz to 10 kHz) and over greater distances (50–100 m electrode arrays are common), often on an open domain (the Earth's surface) or in bore-holes, and encounters resistivities which can vary over orders of magnitude across nearby regions. In biomedical EIT, time difference EIT is often preferred, but for geophysical settings, a static reconstruction of the actual resistivity distribution is often required. There are also monitoring applications in which, similar to EIT, changes in resistivity are of interest.

15.2 Common applications

As in biomedical EIT, the basic DC geoelectrical resistivity measurement configuration comprises four electrodes connected to a resistivity meter, with two passing current (labelled A,B; C1,C2; or C+,C-) and two measuring a potential difference (M,N; P1,P2; or P+,P-). Typically many electrodes (up to hundreds) are connected

to the meter simultaneously, and user-defined measurement schedules control which configurations of electrodes are measured in which order. It is often the case that multiple potential difference measurements can be made simultaneously on different pairs of potential electrodes for each current injection ("multi-channel" acquisition). Connections to the electrodes are typically made using multi-core cables with regularly spaced take-outs, and the electrodes are usually stainless steel rods or plates (figure 15.1). Distances between electrodes range from tens of centimetres to hundreds of metres depending on the desired survey area and depth of investigation.

Fig 15.1: Example of an Electrical Resistivity Tomography field survey (BGS © UKRI 2019).

Geoelectrical resistivity meters mostly employ either a switched DC signal, where the current switches from positive to zero to negative to zero to positive over a few seconds, or low-frequency AC signal between 1 Hz and tens of Hz. Signal processing is either performed by the instrument or the full waveform may be recorded for later analysis. Switched DC systems tend to require more power (of the order of 100 W), whilst low-frequency AC systems, using lock-ins or digital signal processing, are usually more efficient (of the order of 10 W). Field systems are usually powered from automotive batteries, with typical applied voltages of tens to hundreds of volts driving currents of tens to hundreds of milliamps between the current electrodes. The ratio of the applied voltage and the injected current is usually dominated by the contact impedance at the electrodes, which depends on the surface area of the electrodes, the resistivity of the surrounding earth material, and the degree of galvanic contact between the two. Contact resistances can be lowered by using larger electrodes with greater surface area. Normally in ERT applications the electrode dimensions are much smaller than the spacing between electrodes. Most geoelectrical inversion algorithms treat the electrodes as point-like. In instances where contact resistances are too high, it is more common to reduce them by treating the ground in the immediate vicinity of the electrode, often using water, saline solution, or conductive slurries or gels, rather than using larger electrodes. Reducing the contact resistance increases the signal-to-noise or, conversely, may justify reducing the required power. Some systems can run from generators and apply greater voltages for use in highly resistive environments. It is also possible to

use physically separated current and potential bipoles with high power systems to enable larger scale (multi-kilometre) surveys.

Unlike biomedical applications, in geoelectrical surveying it is rarely possible to place electrodes over an entire boundary surrounding the region of interest. Most investigations are undertaken using either lines or grids of electrodes on the ground surface of the area to be surveyed, or, less commonly, lines of electrodes deployed in boreholes. The positions of these electrodes must be accurately recorded (either by GPS or other surveying techniques, e.g. tape). Geoelectrical surveys usually comprise sets of measurements made in one or more standard configurations (figure 15.2) with a range of bipole lengths and spacings. It is sometimes possible to deploy electrodes sufficiently far from the survey area to be practically at infinity, which enables the use of pole-pole and pole-dipole measurements.
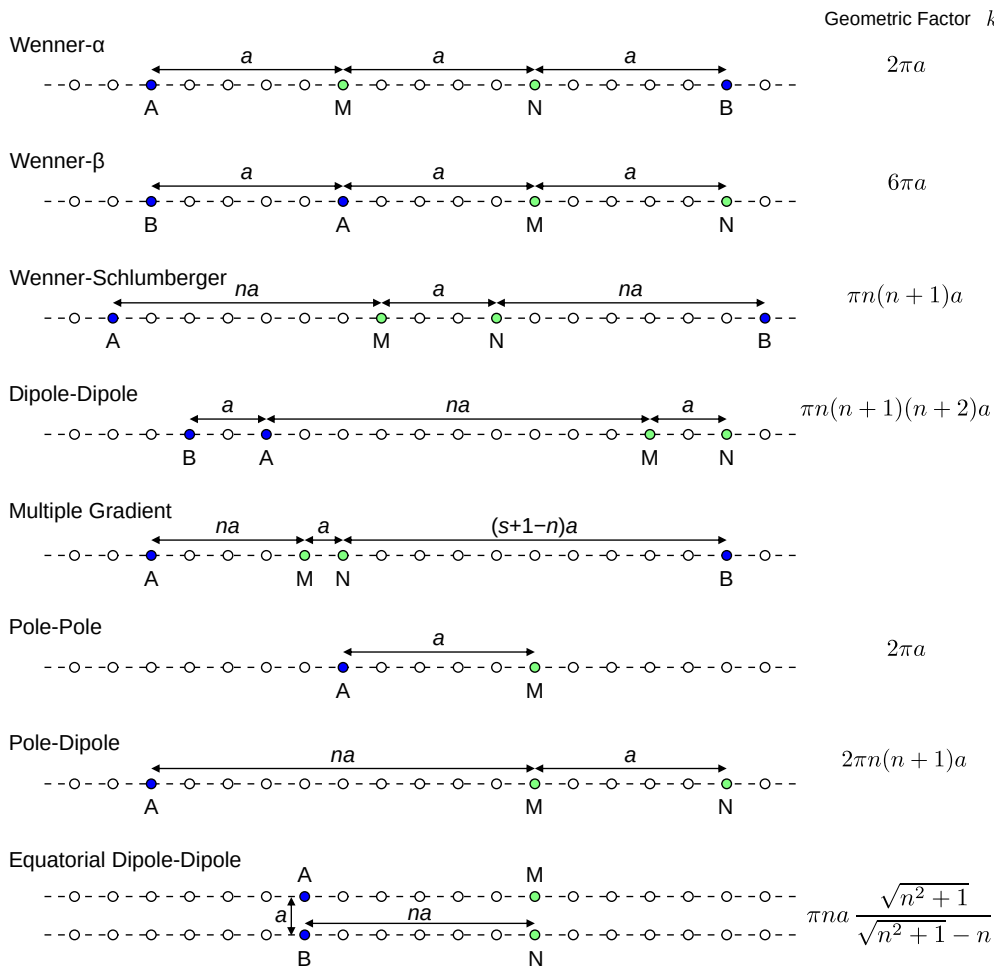

Fig 15.2: Commonly used ERT survey configurations showing current electrodes (A,B) in blue ● and potential electrodes (M,N) in green ○. The factors n and s are typically integer multipliers ≥ 1 of the electrode spacing a and specify the lengths and spacings of the bipoles; geometric factors k from equation (15.2) are shown adjacent to selected configurations where a simple expression exists (BGS © UKRI 2019).

For quick interpretation of raw data, the measured transfer resistance R can be multiplied by a geometric factor k (figure 15.2, right-hand column) based on the assumption of a homogeneous flat half-space, giving a quantity known as the apparent resistivity ϱ_a. This provides a simple check of the range of resistivities present in the subsurface and the approximate locations of structures of interest. The apparent resistivity also normalizes measurements so that they are more equally

weighted in the reconstruction (see §15.12).

For an electrode at the surface of a half-space, current I causes a radial potential $\phi = \rho I / 2\pi r$ in a medium with homogeneous resistivity ρ at radial distance r from the electrode. Note that there is a singularity at the electrode when $r = 0$. A dipole created by current flowing between source electrodes A and B (figure 15.2) causes a potential ϕ measured at electrodes M and N as ϕ_M and ϕ_N. A surface ERT measurement V is the difference between these potentials at the two measurement electrodes $\Delta\phi$

$$\phi_M = \frac{\rho I}{2\pi}\left(\frac{1}{AM} - \frac{1}{MB}\right) \qquad \phi_N = \frac{\rho I}{2\pi}\left(\frac{1}{AN} - \frac{1}{NB}\right)$$

$$V = \Delta\phi = \frac{\rho I}{2\pi}\left(\frac{1}{AM} - \frac{1}{MB} - \frac{1}{AN} + \frac{1}{NB}\right) \tag{15.1}$$

where each distance AM, MB, AN, NB is between the corresponding stimulus electrode A or B and a measurement electrode M or N. The model may be applied for any arbitrary pair-wise electrode placement. Buried electrodes may be handled by placing "mirror image" electrodes at an equal distance above the flat surface to correct for boundary effects [3, 4].

Equation (15.1) may be rearranged to find the apparent resistivity $\rho \to \varrho_a$ as an estimate of the homogeneous resistivity given a single measurement

$$\varrho_a = \frac{V}{I} k = Rk \qquad \text{for } k = \frac{2\pi}{\left(\frac{1}{AM} - \frac{1}{MB} - \frac{1}{AN} + \frac{1}{NB}\right)} \tag{15.2}$$

where $R = V/I$ is the measured transfer resistance as the ratio of a measured difference in potentials V resulting from an applied current I. A geometric factor k accounts for the electrode configuration. The resistivity is "apparent" because inhomogeneity in the medium, electrodes with finite size, or a surface that is not flat introduce errors. The geometric factor k may also be calculated as a normalization factor from an arbitrary geometry by calculating the measurements for a homogeneous $1\,\Omega$m model $k = 1/\mathcal{F}(1)$ using a FEM forward model $\mathcal{F}$ with $1\,$A (unit) stimulus.

More quantitative interpretation requires solving the inverse problem. How this is parametrized depends on the geological setting, the placing of the electrodes, and the types of measurements made. In the simplest case, where the subsurface structure is horizontally layered, Wenner measurements can be made on a line of electrodes with a range of bipole lengths and centred on the same point. This is known as vertical electrical sounding, and can be inverted using a 1D-model where the resistivity varies only as a function of depth. More commonly, a survey line will be placed perpendicular to the strike[1] of the subsurface structure. Then the assumption can be made that the resistivity varies with depth and the distance along the line, but not in the perpendicular direction. The inverse model is then a 2D parametrization (although it represents a 3D structure). Unlike biomedical EIT, the current flow is treated as 3D from point electrodes, so the resulting model is referred to as a 2.5D solution (see §15.10). Lastly, measurements can be taken on a 2D surface grid (see §15.3). Often there will not be sufficient numbers of electrodes

---

[1]Strike (compass heading) and dip (steepest angle) define a unit vector orientation of the layered rock, for example sedimentary layers rotated by faulting or other deformation processes relative to a flat horizontal layer.

available to emplace the whole grid at once, so multiple linear surveys are carried out along parallel lines. For better results with 3D inversion, it is good practice to include at least some lines in the perpendicular direction (referred to as tie-lines) and along diagonal directions. If more than one parallel line of electrodes can be laid out at once, then true 3D measurements (such as equatorial dipole-dipole) can also be used.
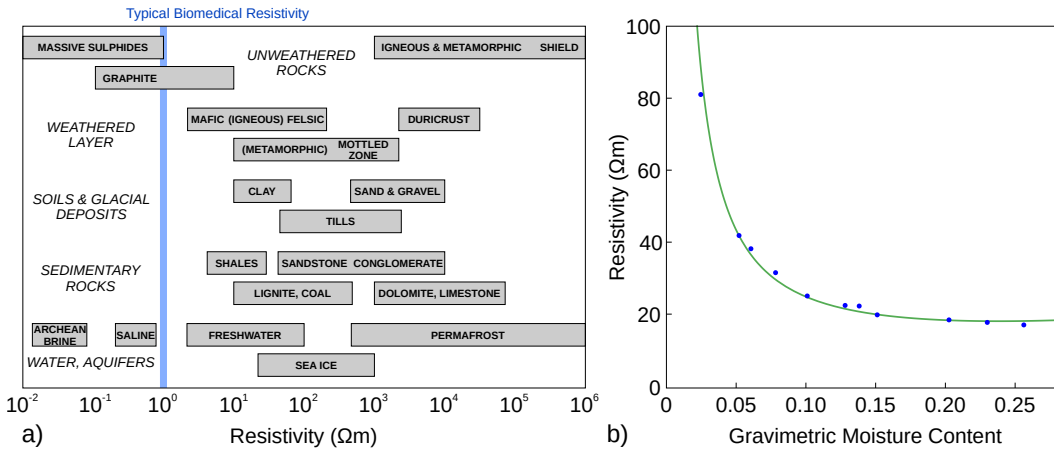

Fig 15.3: Material and moisture content affect resistivity; a) approximate resistivity ranges for surface waters, rocks and soils; b) example of petrophysical relationship between resistivity and moisture content of a porous material showing data and fitted model (BGS © UKRI 2019).

Geoelectrical surveys are widely used because the resistivity of the earth is sensitive to a wide range of properties of interest to geoscientists. Predominantly the resistivity varies strongly with lithology (rock type) over a range of many orders of magnitude (figure 15.3a). It also depends on the weathering of the rock, its fracturing, its degree of saturation with fluids, the ionic content of saturating pore fluids, its temperature, and the presence of contaminants and pollution. Consequently the results of geoelectrical surveys are often transformed into other subsurface properties of interest (such as moisture content) via petrophysical relationshipsThese can be determined experimentally by recording the resistivity as a function of the target parameters in representative samples, and fitting petrophysical models (figure 15.3b), such as Archie's Law for sands, gravels and sedimentary rocks, or the Waxman-Smits or Dual Water models where significant clay mineralization is present [5, 6, 7].

Their wide applicabilitymeans that geoelectrical surveys are rarely undertaken without significant ground-truth being acquired (or already available), since interpretation is otherwise difficult and open to question. Types of commonly used ground truth, prior information and calibration include geological maps and ground models, topographic surveys, trial pits, borehole logs, water level loggers (piezometers), point sensors (measuring local electrical conductivity, moisture content and temperature), tilt sensors, accelerometers, other geophysical survey methods (e.g. ground penetrating radar, seismics, microgravity), and laboratory testing and calibration of material samples to develop petrophysical relationships between resistivity and parameters of interest (e.g. moisture content).

There are many and varied applications of geoelectrical imaging, including geological mapping and ground model development; hydrology and hydrogeology (e.g. marine, rivers, aquifers); natural hazard detection and mitigation (e.g. land-

slides, sinkholes); geotechnical and engineering hazards (e.g. slope stability); detection and mapping of voids (e.g. caves, tunnels, mineshafts); mineral prospecting and resource assessment; contaminated land / brownfield site investigation (e.g. landfills, leachate plumes, groundwater pollution); and archaeology. Several review papers from the last decade or so are available which cover the methods and applications in detail [8, 9, 10, 11, 12, 13].

15.3 Research applications

Ongoing research and development into geoelectrical methods has seen advances in instrumentation and inversion algorithms, which have led to a rapid expansion in applications beyond standard, widely used 2D resistivity surveys. Some examples of recent developments are the increased use of large numbers of electrodes in surface grids for full 3D imaging; time-lapse/4D data acquisition and inversion for monitoring processes; optimal selection of measurements and electrode locations to maximise image resolution; subterranean electrodes to improve image resolution at depth; joint inversion of complementary geophysical data; accommodating changes in boundaries and electrode locations over time; and capacitively coupled electrodes for highly resistive environments. 3D geoelectrical imaging relies on a combination of a 3D inverse model, typically finite-element or finite-volume and parametrized into hexahedral or tetrahedral model cells, and data measured on a grid of electrodes at the surface. As noted in the previous section, it is common to collect such data using a small linear array, comprising a few tens of electrodes, making multiple parallel linear surveys and combining the data for inversion. In this case, the parallel surveys should not be separated by more than two or three times the electrode spacing along the line [14], and some perpendicular tie-lines should be included. Such acquisitions schemes can cause directional artefacts in the resulting images. These can be avoided if several parallel lines of electrodes, or ideally the entire grid, can be emplaced simultaneously permitting the collection of more general planar configurations as well as collinear measurements aligned in different directions (figure 15.4).

Since laying out arrays with larger numbers of electrodes for 3D surveys can be time-consuming, it is often desirable to install the electrodes in a semi-permanent manner, especially if repeat surveys of the same site are needed to monitor changes. This usually involves burying the array a few centimetres below the ground surface to protect the electrodes and wiring from mechanical damage. Sometimes the galvanic contact with the ground can be poor if the surface is dry or rocky, in which case the immediate vicinity of the electrodes can be treated using conductive slurries, gels or grouts to temporarily reduce the contact resistances. The array can then be connected periodically to a survey resistivity meter, or permanently to one of a growing number of geoelectrical monitoring systems (figure 15.5a). These are used to collect repeated data sets, which are inverted to produce models of the changes in resistivity over time (figure 15.5b). Several types of time-lapse inverse method are available [16]. These include inverting directly for the changes in the data, or imposing constraints between the current model and a baseline. Both of these approaches require a well-characterised baseline data set and background model. Another approach is to invert all the data sets as a 4D model with temporal constraints between subsequent time steps similar to the spatial constraints between adjacent
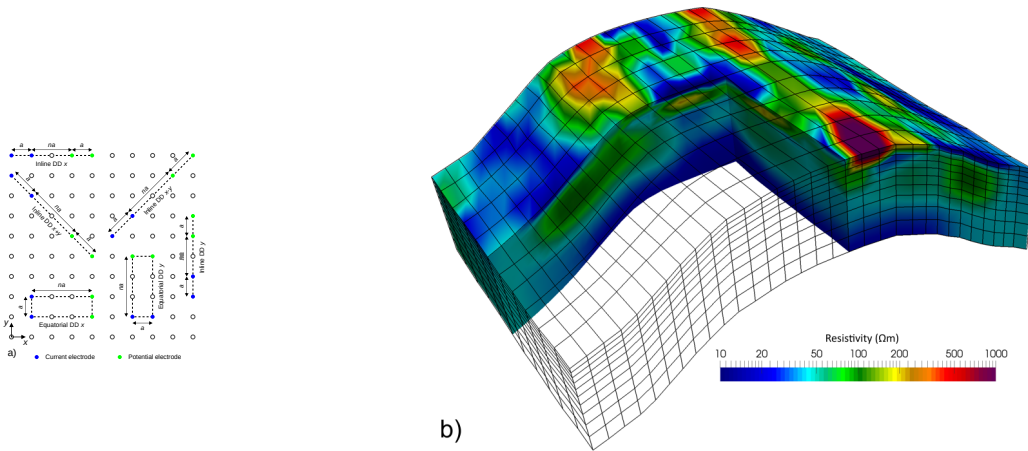
Fig 15.4: a) Examples of full 3D survey measurement types comprising inline and equatorial dipole-dipole configurations with different orientations; b) Example of a 3D resistivity model comprising hexahedral cells generated from a geoelectrical survey on a grid of 12×32 electrodes [15] (BGS © UKRI 2019).

model cells. This places no emphasis on any particular time step, and so does not require extra effort to characterise the baseline data and background model.
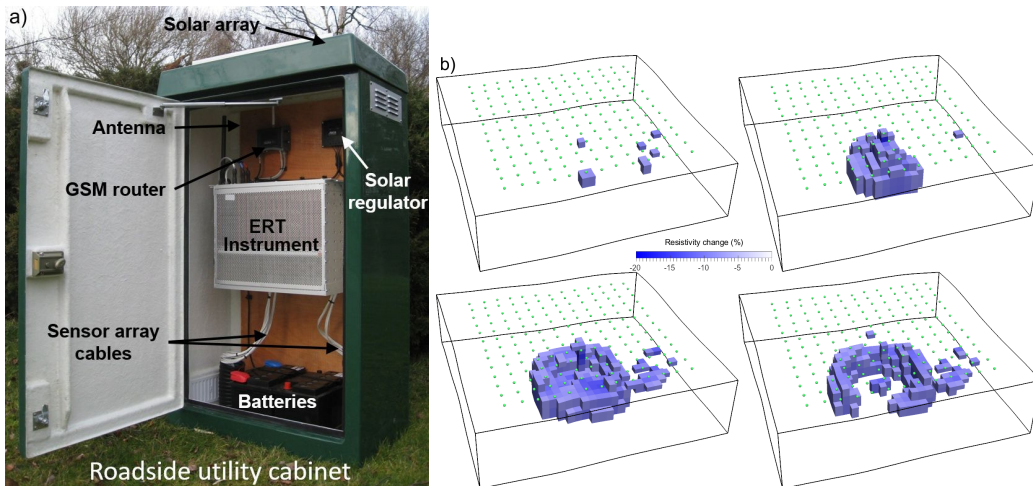

Fig 15.5: a) Permanently installed geoelectrical monitoring system, comprising ERT instrument, communications, batteries, solar panel and connections to electrode arrays; b) Relative change images from 4D inversion of ERT monitoring data taken from a grid array (green dots) above a simulated utility pipe leak, showing regions of model with resistivity changes $< -7.5\%$ (BGS © UKRI 2019).

Since the most common causes of changes in the ground resistivity are variations in the degree of saturation and quality of the groundwater, there has been rapid growth in the use of time-lapse / 4D ERT to monitor hydrological processes. Example fields of application include landslide hydrology, earthwork stability, dam integrity, CO_2 sequestration, landfills, contaminated ground, nuclear waste decommissioning, leak detection, permafrost, aquifer exploitation, agriculture and soil/plant science, geothermal systems, and tracer tests. Details of these and other applications can be found in recent review papers [17, 9, 10, 18, 12, 19].

Geophysical monitoring encounters a range of seasonally varying surface temperatures which directly affect ionic mobility, and therefore resistivity, by approximately 2%/°C near 25°C. Biomedical EIT does not generally encounter large temperature variation courtesy of the body's tight thermal regulation. On freezing, water solidifies into crystalline ice which drastically increases resistivity. Below ground, temperatures vary as a time delayed sinusoid that decays with depth and is balanced by steady heat radiated from below. Homogeneous models of this heat conduction are often sufficient to correct for seasonal variation in long-term monitoring data [15] particularly when validated against thermal depth arrays (e.g. thermistors).

As with biomedical EIT, a fundamental limitation of the technique is that image resolution decreases rapidly as the distance from the electrodes is increased. Since most geophysical applications use surface electrodes, this typically means that resolution decreases with depth. There has been considerable interest in the last 10–15 years in using optimal experimental design techniques to maximise resolution in more poorly resolved regions of the model, ideally without increasing survey time. Several approaches have been explored to maximise the resolution of the reconstructed image including reconstructing comprehensive data sets from a linearly independent complete subset; maximising the sum of the Jacobian sensitivity matrix elements; maximising the sum of the model resolution matrix elements; minimizing the average of the point spread function; and maximising the determinant of the normal matrix (see [20] and references therein). The methods involving the model resolution matrix have received the majority of the research effort, and have been applied to 2D and 3D survey design, including investigations with subsurface electrodes (see [21] and references therein). The resulting surveys require care to use in practice due to the types of multichannel instrumentation available and the effects of electrode polarisation [20], but they have been shown to produce images with measurably better fidelity, especially in poorly resolved regions such as the base, edges and corners of the models (figure 15.6 left images). Similar techniques have also been used to produce adaptive measurement schemes for time-lapse geoelectrical monitoring [22], and to optimise the placement of electrodes in arbitrary arrangements for non-standard 2D and 3D surveys [23, 24].

A different way to improve the resolution at depth is to implant electrodes beneath the ground in the vicinity of the imaging region, and make measurements using combinations of all surface, all subsurface, and subsurface-to-surface electrodes [25]. This is most commonly done by installing electrodes in boreholes [26], but other approaches include direct-push electrodes [27, 28] or placing electrodes in void spaces below ground (e.g. on tunnel walls: [29, 30]). Figure 15.7 shows an example of using resistivity measurements between boreholes to investigate the flow and dispersal of a tracer test in a confined aquifer [31].

The fidelity of inverse images can also be improved by jointly inverting data sets from different geophysical techniques, since their resolution and sensitivity to subsurface features are often complementary. Various approaches have been taken, depending on the types of data available. If the techniques depend on the same property, but cover complementary regions of the model with different sensitivities, they can be inverted together directly [32]. In cooperative joint inversions, data are inverted separately for different parameters but derived information, such as structure, are exchanged [33, 34, see figure 15.6 right image]. Other approaches couple the inversions together via the spatial structure of the parameter distributions ([35]
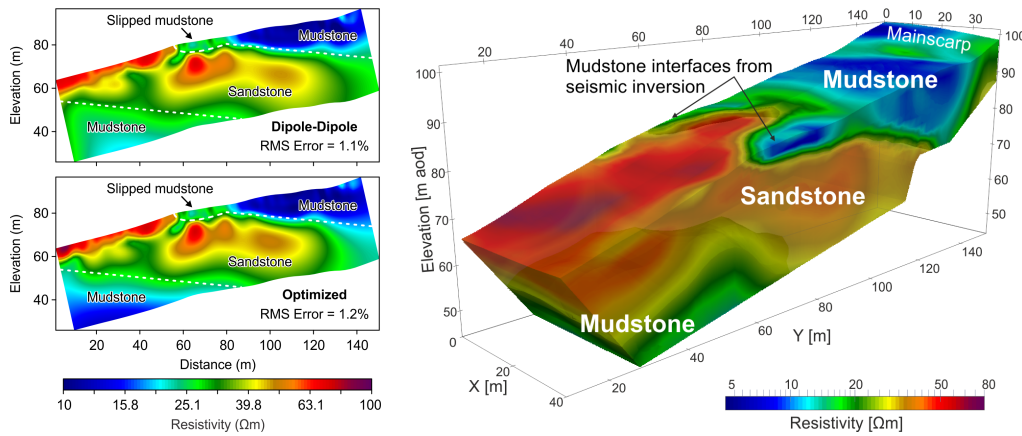
Fig 15.6: Comparison of standard dipole-dipole (above left) and optimized (below left) survey images of a landslide. Both images capture the geological structure but in the optimized image the sandstone/mudstone interfaces are better resolved; (right) 3D ERT image of the same landslide where the structure of the interface between the upper mudstone layer and the sandstone was obtained from a seismic refraction inversion and incorporated as structural information in the ERT inversion (BGS © UKRI 2019).

and references therein) or via petrophysical relationships that relate the multiple geophysical parameters to some common property such as the porosity ([36] and references therein; [37] and references therein).
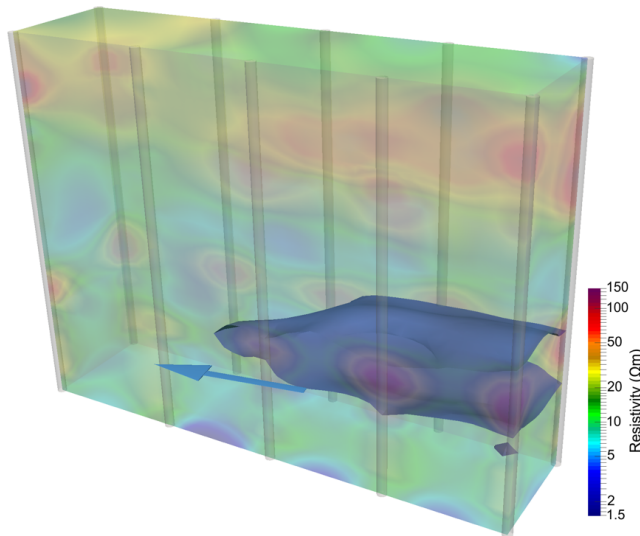

Fig 15.7: Isosurface (blue) showing regions of resistivity model changed by $< -20\%$ due to the injection of a conductive tracer in a confined aquifer. Each borehole (grey cylinder) contained 16 equally spaced electrodes at $0.5\,\text{m}$ depth intervals (BGS © UKRI 2019).

A particular type of challenge that can cause artefacts in ERT image reconstruction is that of changes to the boundary on which the electrodes are installed. If these changes can be measured and recorded, they can be incorporated into the inversion and their adverse effects minimised e.g. mapping fissures at length scales smaller than the electrode spacing [38] or measuring the displacements of electrodes during ground movements such as landslides [39, 34] or shrink-swell [40]. In particular, the application of ERT to landslide monitoring has led to inverse methods that incorporate electrode positions as model parameters to be reconstructed [41, 42, 43] in much the same way as in lung function EIT imaging.

For certain applications, e.g. on dry, frozen or paved surfaces, galvanic contact impedances can be so high that they prevent injection of sufficient current for a reliable signal. In such cases, capacitively coupled systems can be used that employ non-grounded electric dipoles. They operate in a quasi-electrostatic regime typically at audio frequencies (10-20 kHz), in which the DC resistivity inversions can be applied [44]. Capacitive resistivity systems have been used for rapid acquisition of data on resistive surfaces using towed arrays [45, 46], for assessing the strength of heritage stonework [47], and for monitoring of freeze-thaw cycles in permafrost [48].

15.4   Complex resistivity and induced polarization

In biomedical applications of EIT, the quadrature component of the voltage is usually very small, and below the resolution of the instruments. In geophysics, the phase shift between the measured voltage and applied current for certain materials can be appreciable (up to several hundred milliradians). The phase shifts result from the reversible accumulation of charges, and the effects can be observed and measured in either the time- or frequency-domain. In the time-domain the technique is known as Induced Polarization (IP) and is measured by integrating the decaying residual voltage after current switch-off and normalizing by the initial DC voltage. This gives a dimensionless measure of the apparent chargeability in mV/V (or permille). In the frequency domain, the technique is referred to as either Complex Resistivity, if working at a single frequency, or Spectral Induced Polarization (SIP), if measuring over a range of frequencies. IP techniques were first applied in the exploration industries, but more recently have been used in environmental applications ([49] and references therein).

IP measurements should ideally be made using non-polarizing electrodes with shielded cables. Nonetheless, in many practical circumstances good data can be collected using the same multi-core cables and stainless steel electrodes as used in resistivity surveys. Having the current and potential electrodes on separate cables will improve the data quality if capacitive coupling in the multi-core cables is significant, e.g. when contact impedances are high [50]. Consequently, IP surveys are often carried out using the same equipment as for resistivity surveys, but they take longer due to the signal-to-noise ratio usually being significantly smaller. IP effects can arise from several mechanisms [51], but the predominant ones are electrode polarization and membrane polarization. Electrode polarization is caused by charge build up when electrolytic current flowing though the pore water is impeded by conductive mineral grains, through which the current has to flow electronically. Membrane polarization is largely caused by clay minerals which possess a negative surface charge that attracts positive ions and impedes electrolytic flow through narrow pores. Chargeability effects in the ground can be caused by materials like metals, metallic ores, clays, landfill waste, and hydrocarbons.

Different inverse methods have been used and researched for induced polarization data, depending on the type. For time-domain measurements in terms of apparent chargeability, the data are inverted with the apparent resistivities to give a resistivity and a chargeability model of the ground (figure 15.8). If the full voltage waveforms are recorded, parameters for empirical spectral models can be extracted
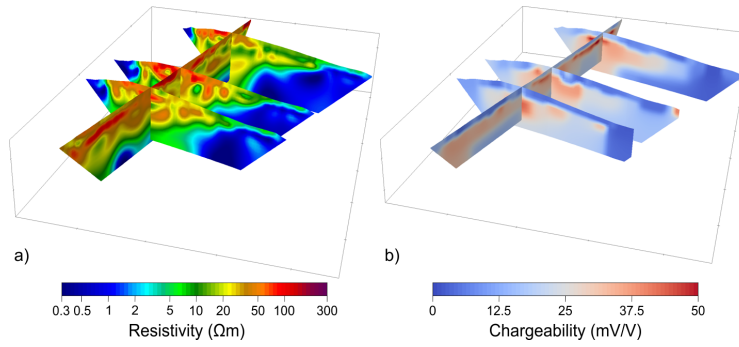
Fig 15.8: a) Resistivity image of a coastal embankment with a core containing household waste. b) The waste materials in the core have a high chargeability signature (BGS © UKRI 2019).

[49, 52]. In the frequency domain, the data are inverted for a complex resistivity ground model, either directly or by decoupling the real and imaginary components [53]. If data are available at several frequencies (SIP), then spectral model parameters can be fitted to the observed dispersion data.

15.5   Logarithmic parametrization

Two numerical problems can occur if geophysical resistivity reconstructions are attempted blindly. First, non-physical negative resistivities can be reconstructed which can then skew nearby regions of the reconstruction. Second, the resistivities tend to span orders of magnitude which makes it difficult to apply effective regularization to the reconstruction. Both issues are addressed by converting to a log parametrization. A transformation to log units allows an unconstrained reconstruction, for example using iterative Gauss-Newton methods, to solve a constrained problem. The transform must be injective, which is to say that there is a one-to-one mapping of values in the new and old parameter spaces.

It is more common to use resistivities for geophysical applications, but in the following we use the conductivity parameters familiar to biomedical EIT. To restrict solutions to positive valued conductivities ($\sigma > 0$), we can apply a log parametrization $\mathbf{p}$ where

$$\mathbf{p} = g \ln \sigma \qquad \longleftrightarrow \qquad \sigma = \exp\left(\frac{\mathbf{p}}{g}\right) \qquad \text{for } g > 0, \quad 0 < \sigma < \infty \qquad (15.3)$$

with natural log $\ln$: $g = 1$ and base-10 $\log_{10}$: $g = 1/\ln(10)$. In a Gauss-Newton iteration the transformation is first used to convert the conductivity to the log parameter space, update the parameters using the Jacobian, then take the inverse transform to check data misfit (line search and stopping criteria) using the forward model.

The Jacobian for the new log parameter space is computed from the chain rule

$$\mathbf{J}_{\mathbf{p},i,j} = \frac{\partial \mathbf{b}_i}{\partial \mathbf{p}_j} = \frac{\partial \mathbf{b}_i}{\partial \sigma_j} \frac{\partial \sigma_j}{\partial g \ln \sigma_j} \qquad\qquad \mathbf{J}_{\mathbf{p}} = \mathbf{J}_\sigma \frac{\text{diag}(\sigma)}{g} \qquad (15.4)$$

for the i-th measurement $\mathbf{b}_i = V_i$ and j-th conductivity element σ_j, so that the original Jacobian columns are scaled by the conductivity σ at which the Jacobian was

calculated and g is, as above, selects the type of log scaling. In this parametrization for resistivity ρ, one can either directly substitute $\sigma \to \rho$ resulting in an inverted weighting and regularization scheme, or translate the equations $\sigma = 1/\rho$ to get the equivalent numerical result in terms of resistivity.

15.6 Absolute reconstruction

The term "absolute reconstruction" is somewhat misleading, as it does not refer to the resistivity being greater than zero, which can be achieved by using the log parametrization (see §15.5). Instead, the term refers to a reconstruction using a single set of measurements rather than a time or frequency difference reconstruction. (Again these equations are written in terms of conductivity σ here, but are typically written in terms of resistivity ρ in geophysical contexts.) The most common approach is to use a Gauss-Newton iterative update, for which the left-hand side of the update $\delta\sigma$ looks identical to the Gauss-Newton single-step solution used in time-difference EIT. On the other hand, the right-hand side differs by requiring terms that are most often dropped from the single-step solution, as they are set to zero. To arrive at a solution, one iterates through the following two equations

$$\delta\sigma = (\mathbf{J}^\mathsf{T}\mathbf{W}\mathbf{J} + \lambda^2\mathbf{Q})^{-1}\left(\mathbf{J}^\mathsf{T}\mathbf{W}\left(\mathbf{b} - \mathcal{F}(\sigma_n)\right) + \lambda^2\mathbf{Q}(\sigma_n - \sigma_*)\right)$$
$$\sigma_{n+1} = \sigma_n + \alpha_n\,\delta\sigma \tag{15.5}$$

for Jacobian $\mathbf{J}$, inverse measurement covariance $\mathbf{W}$, regularization $\mathbf{Q}$ scaled by hyperparameter λ, prior conductivity estimate σ_*, measured data $\mathbf{b} = [V_1\ V_2\ \ldots\ V_n]^\mathsf{T}$, current conductivity estimate σ_n, and forward model of the measured data at that conductivity estimate $\mathcal{F}(\sigma_n)$. The prior conductivity estimate is often set to the initial conductivity estimate ($\sigma_* = \sigma_0$). The update direction $\delta\sigma$ gives a search direction. A line search may be used to find an "optimal" step size $0 < \alpha_n < 1$ or various heuristics are available, for example ($\alpha_n = 1$). Line searches are expensive to compute, since they require multiple calculations of the forward model, but can significantly improve convergence rates and solution accuracy.

The Jacobian should be recalculated at each σ_n when conductivities change significantly: current density through the domain changes as conductivities are modified, resulting in changes to the regional sensitivity $\mathbf{J}$. This is also the key reason why absolute reconstructions are most often a necessary first step in any time-difference solution for ERT datasets: a Jacobian calculated on a homogeneous conductivity can be wildly incorrect when conductivities vary over the ranges commonly observed in the near surface.

We can observe that the forward model $\mathcal{F}(\sigma_n)$ now enters the picture, where it would otherwise cancel out in time-difference EIT. The fact that the forward model plays a key role in the absolute reconstruction indicates that model errors such as electrode placement, electrode movement, boundary or contact impedance are now critical factors in a successful reconstruction.

Absolute solutions are much more computationally expensive to reconstruct than typical EIT single-step time-difference reconstructions. The majority of the computational time is spent re-calculating the Jacobian used in the update $\delta\sigma$ and forward solutions for the line search α at each iteration.

Iterations are halted at "stopping criteria" which can be an iteration limit, when the total misfit is sufficiently reduced, or when progress slows. The hyperparameter is sometimes modified as iterations proceed, which introduces "trust region" type iterative solutions.

An initial conductivity estimate σ_0 is required as a starting point. As with most iterative algorithms, the starting point can determine what sorts of solutions can be found as the algorithm may become trapped in local minima as it traverses away from the initial estimate. The most common approach is to take the mean of the apparent resistivities, which works by using the scaling from a homogeneous $1\,\Omega$m resistivity used in the forward model $\mathcal{F}(1) = 1/k$ geometric factor k, so that

$$\rho_0 = \frac{1}{n} \sum_{i=1}^{n} \frac{V_i}{I_i} k_i \tag{15.6}$$

where the single scalar resistivity ρ_0 value gives a best-fit homogeneous estimate of conductivity $\sigma_0 = 1/\rho_0$ from the measurements $\mathbf{b}_i = V_i$. The initial estimate can be thrown off by outlier apparent resistivities, which can be treated by discarding or de-weighting based on an error model (see §15.11).

15.7   Timelapse inversion

Timelapse inversion in ERT differs from time-difference EIT, in that the changes can be non-linear enough to require iterative updates. The absolute conductivity Gauss-Newton solution (15.5) is modified so that the data and conductivity represent differences $\mathbf{b}_\Delta = \mathbf{b}_t - \mathbf{b}_{t=0}$ and $\sigma_\Delta = \sigma_t - \sigma_{t=0}$ from a reference time $t = 0$, often the solution of an absolute reconstruction. This expansion leads to a timelapse Gauss-Newton iterative formulation over the data misfit $\mathbf{d}$ where

$$\mathbf{d} = (\mathbf{b}_t - \mathbf{b}_{t=0}) - (\mathcal{F}(\sigma_t) - \mathcal{F}(\sigma_{t=0})) = \mathbf{b}_\Delta - (\mathcal{F}(\sigma_{t=0} + \sigma_{\Delta,n}) - \mathcal{F}(\sigma_{t=0}))$$

$$\delta\sigma_\Delta = (\mathbf{J}^\mathsf{T}\mathbf{W}\mathbf{J} + \lambda^2\mathbf{Q})^{-1} \left(\mathbf{J}^\mathsf{T}\mathbf{W}\mathbf{d} + \lambda^2\mathbf{Q}(\sigma_{\Delta,n} - \sigma_{\Delta,*}) \right)$$

$$\sigma_{\Delta,n+1} = \sigma_{\Delta,n} + \alpha_n \, \delta\sigma_\Delta \tag{15.7}$$

and, as with time-difference EIT, it is often reasonable to initially assume no change in conductivity ($\sigma_{\Delta,*} = \sigma_{\Delta,0} = 0$) [54]. The same absolute reconstruction code can often be used to calculate a timelapse solution with a few trivial modifications because the changes are entirely related to the data misfit term $\mathbf{d}$. An alternate approach is to regularize the temporal changes simultaneously through a Kronecker expansion of the Gauss-Newton update (15.7) over multiple frames [55, 56, 16].

If one assumes no line search ($\alpha_n = 1$), one iteration, and a "no change" initial estimate, then the above formulation simplifies to the familiar time-difference EIT equation for a single-step Gauss-Newton solution

$$\sigma_\Delta = (\mathbf{J}^\mathsf{T}\mathbf{W}\mathbf{J} + \lambda^2\mathbf{Q})^{-1}\mathbf{J}^\mathsf{T}\mathbf{W} \, (\mathbf{b}_t - \mathbf{b}_{t=0}) \tag{15.8}$$

though these simplifications are often inappropriate in the presence of large underlying variations in conductivity. In biomedical EIT, where the body is largely constrained to a relatively narrow range of conductivities due to intra- and extra-cellular fluids and the body's regulation of salinity, these assumptions are much more reasonable.

15.8   The use of electrode models

In geoelectrical applications, the electrodes tend to be small in comparison to the separations between them. This means that they can usually be modelled as point sources. [57] showed that for rod electrodes, a Point Electrode Model (PEM) is adequate for electrode lengths of up to 20% of the unit electrode separation. By contrast, in most biomedical applications a Complete Electrode Model (CEM) has to be used to account for the finite size of the electrode. Larger electrodes are sometimes used, e.g. to reduce contact resistance (often in highly resistive environments, or in small-scale laboratory work where point-like electrodes would be too small to provide good galvanic contact). In these cases, the finite size of the electrodes must be taken into account. If the electrode geometry is simple, such as a ring [58] or ellipsoid [59], the effects can be calculated analytically. For more general cases, CEMs have been developed for the 3-D [57] finite element formulation of the forward and inverse problems, although the 2.5-D problem has not been tackled convincingly. For induced polarization/complex resistivity, the CEM is often found to be an important ingredient in reconstructions because the electrode contact can strongly influence measurements. Simpler approaches, which are sufficient if the contact impedance is small, are to model the electrode as a point source embedded in a highly conductive region [60] or as an extended perfect conductor [61]. A small number of studies have used CEM techniques to analyse field and laboratory data [62, 63, 64, 42].

15.9   Modelling open domains

A major difference between the biomedical and geoscientific applications of EIT is that the former make measurements on a bounded surface (the patient), whereas the later are frequently applied to open domains (in field applications, although laboratory tank experiments and sample investigations are bounded). Open domains typically consist of the ground surface, at which Neumann boundary conditions are applied, and a far subsurface boundary effectively at infinity. An early approach to treat this boundary was to impose a Robin condition

$$\frac{\partial \phi}{\partial \mathbf{n}} + \alpha \phi = 0 \tag{15.9}$$

on a nearer, artificial subsurface boundary with outward normal $\mathbf{n}$ such that the potential ϕ has a $1/r$ behaviour at a distance r from the electrode [65]. The parameter $\alpha = (\mathbf{n} \cdot \mathbf{r})/r^2$ with $r = ||\mathbf{r}||$ for a surface current electrode [66] and $\alpha = (r'^3 \mathbf{n} \cdot \mathbf{r} + r^3 \mathbf{n} \cdot \mathbf{r}')/(r^2 r'^2 (r + r'))$ for a buried current electrode [67], where $\mathbf{r}$ is the vector from the electrode to the boundary element and $\mathbf{r}'$ from the electrode's mirror image above the surface to the boundary with $r' = ||\mathbf{r}'||$. The parameter α is, in part, related to $\cos\theta = (\mathbf{n} \cdot \mathbf{r})/r$ for the angle θ between $\mathbf{r}$ and $\mathbf{n}$. These calculations make use of the analytic half-space model of ERT (15.1).

A single boundary condition for all electrode source positions is often sufficient when boundaries are far from sources and sources are close to each other (avoiding updated boundary conditions for each electrode stimulation pair) by taking the average electrode position [65]. For many geophysical settings with apparent topological relief, the overall surface variation from a flat surface is sufficiently small

to make these approximations useful. For example, many hillsides tend to lie at a roughly uniform angle of repose over hundreds of meters (a typical ERT survey length), despite having a significant slope. Rotating the model domain to match this average slope will remove the majority of the topological error in the boundary condition.

Another approach, which has become more common as computer power has increased, is to move the artificial subsurface boundary to a suitably large distance from the electrodes by using progressively larger model cells, such that simply applying either Dirichlet [68] or Neumann [49] boundary conditions is a reasonable approximation to the boundary actually being at infinity. More recently, infinite elements have been used to impose the far boundary condition, improving accuracy and reducing computational load in finite element formulations of the geoelectrical resistivity problem [69, 70].

15.10   2.5D calculations

Two and a half-dimensional (2.5D) solutions are forward problems that are solved in three dimensions under the assumption that one dimension has uniform conductivity from positive to negative infinity with collinear electrodes. In real impedance imaging systems the electrodes are not of infinite length in a particular direction, even when the conductivity distribution is uniform in that direction. The finite size of the electrodes indicates that one cannot correctly approximate three-dimensional solutions with a two-dimensional model unless the electrodes extend to the boundaries, generating a uniform current distribution in the third dimension.

The approach taken in the 2.5D method is to use a 2D FEM, apply a Fourier transform in one dimension, and integrate over the spatial frequencies to obtain a correction, while simultaneously solving the FEM for the other two dimensions [66, 71].

As before, the 2.5D method is presented in terms of conductivity, though resistivity $\sigma = 1/\rho$ is more common in geophysics. By subscripts, the dimensionality of the variables and partial derivatives are denoted, so that a three-dimensional potential ϕ_{xyz} is caused by current at the boundary applied to a three-dimensional conductivity distribution σ_{xyz}. When the conductivity is constant in one dimension z, the partial derivative is zero $\partial\sigma_{xyz}/\partial z = 0$ for constant σ_z and σ_{xyz} is denoted σ_{xy}. For such a conductivity, the potential will vary in the z-dimension.

The z-dependence of the potential ϕ_{xyz} is Fourier-transformed into the spatial frequency domain $\tilde{\phi}_{xy\tilde{k}}$ using the cosine transform and its inverse

$$\tilde{\phi}_{xy\tilde{k}} = \int_0^\infty \phi_{xyz}\cos(\tilde{k}z)dz \quad \leftrightarrow \quad \phi_{xyz} = \frac{2}{\pi}\int_0^\infty \tilde{\phi}_{xy\tilde{k}}\cos(\tilde{k}z)d\tilde{k} \quad (15.10)$$

for a potential that is reflected across the xy-plane so that the potential is an even function $\phi(z) = \phi(-z)$. The conductivity-potential relationship for uniform conductivity in the z-dimension is Fourier-transformed

$$-\nabla\cdot(\sigma_{xy}\nabla\phi_{xyz}) = \frac{\partial\rho}{\partial t}\delta_{xyz} \quad \rightarrow \quad -\nabla\cdot(\sigma_{xy}\nabla\tilde{\phi}_{xy\tilde{k}}) + \tilde{k}^2\sigma_{xy}\tilde{\phi}_{xy\tilde{k}} = \tilde{Q}\delta_{xy}$$
$$(15.11)$$

for a scalar wave number $\tilde{k}$ and steady state current density in the spatial frequency domain with $\tilde{Q}\delta_{xy} = \frac{I\partial\rho}{2\partial t}\delta_{xy} \simeq \frac{I}{2A}$ where [66] have approximated for a shunt electrode with constant current, conducting current I over an electrode area A. The result is a shunt model in the z-dimension and FEM electrode model (PEM, CEM, etc.) in the xy-dimensions.

We note that (15.11) takes the same general form in regular and Fourier space, albeit the spatial frequency domain in place of the z-dimension, with an additional dissipation term dependent on the square of the spatial wave number $\tilde{k}^2$ which suggests an efficient implementation. When assembling matrices for many $\tilde{k}$, only the value of $\tilde{k}$ changes, so the additional 2.5D computations are a small incremental cost relative to the 2D solution.

The potentials found for the forward solution at many $\tilde{k}$ are inverse Fourier transformed and an adaptive quadrature numerical integration is then typically used to accumulate the inverted solutions at appropriate $\tilde{k}$. The first solution $\tilde{k} = 0$ is the two-dimensional solution. For a sufficient summation of $\tilde{k}$, the solution will converge to the three-dimensional solution.
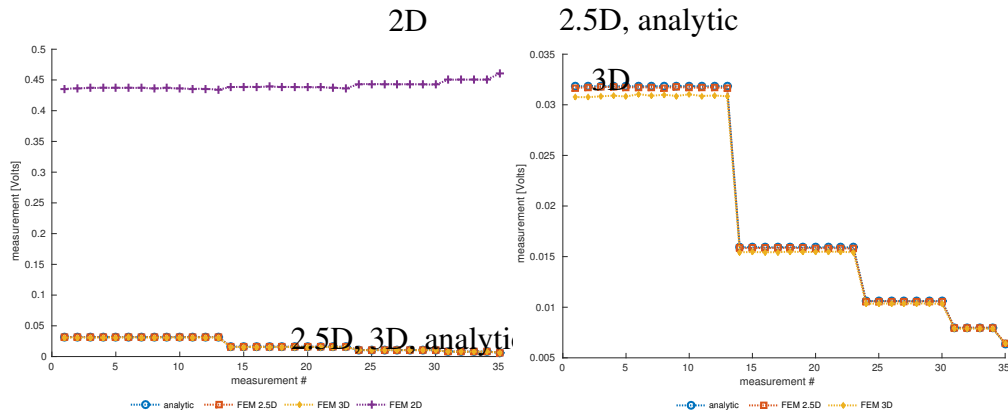

Fig 15.9: 2D versus 3D measurements; a 16 CEM electrode half-space model with Wenner stimulus pattern, models for 2D and 2.5D used the 2D model (half-space, collinear electrode array, equally spaced electrodes), 3D measurements used an equivalent 3D model, and the analytic model used geometry from the 2D model, (a) 2D measurements are significantly different than 3D measurements and the half-space (PEM) analytic model, while (b) 3D, 2.5D and analytic model are in close agreement.

The difference between the 2D and the 3D or 2.5D solutions can be significant as illustrated in figure 15.9, where in 2D widely separated bipoles exhibit simulated measurements in error by as much as 71.5 times their true value. The 2D and 2.5D simulations use the same 2D model (half-space, collinear electrode array, equally spaced electrodes), while the 3D simulations use a 3D model. Both models are 16 electrode CEM half-space models, sharing the same linear electrode arrangement (5 m spacing, 0.1 m diameter), with homogeneous conductivity ($\sigma = 1$). In figure 15.9, the analytic solution (15.1) uses the 2D model geometry and estimates PEM electrodes at the centre of the CEM electrode positions.

The agreement between the analytic, 2.5D and 3D solutions illustrates that the FEM models extend far enough to approximate a half-space without introducing significant truncation errors. The difference between the analytic and 2.5D, and the 3D solution are due to differences in the modelled shape of the electrodes. We do not explore the source of the analytic versus 3D error further here, though in principle it is straightforward to eliminate the possibilities such as PEM versus CEM,

mesh density or electrode shape.

15.11   Data quality measures

Errors in ERT data arise from a number of sources, both systematic and random. It is good practice to try to minimise these errors, and to obtain estimates of data quality to remove outliers and weight the data in the inversion. Sources of systematic error include uncertain electrode locations (through misidentification, poor measurement, or ground movement); electrode polarization effects; damage to cables or electrodes; and cross-talk between cables [72]. Location uncertainties have become less problematic in surface surveys as electrode positions can be readily measured to high accuracy by Global Navigation Satellite System receivers, although positions of borehole electrodes can be harder to determine accurately [73]. Misidentification of electrodes can be checked by measuring sequences of short-offset Wenner or dipole-dipole configurations, which tend to yield negative voltages where electrode cables have been swapped. Ground movements can be accommodated by updated measurement or estimation of the electrode positions [41, 34]. Electrode polarization errors occur when electrodes are used to measure potential soon after passing current but can be mitigated by careful measurement sequencing [20]. Cable and electrode damage are an issue in long-term monitoring installations. In such cases electrodes and cables tend to be installed in protective piping or buried at shallow depth (figure 15.10a), but damage can still occur due to e.g. ground movement, animals chewing through cables (figure 15.10b&c) or human activity [26].
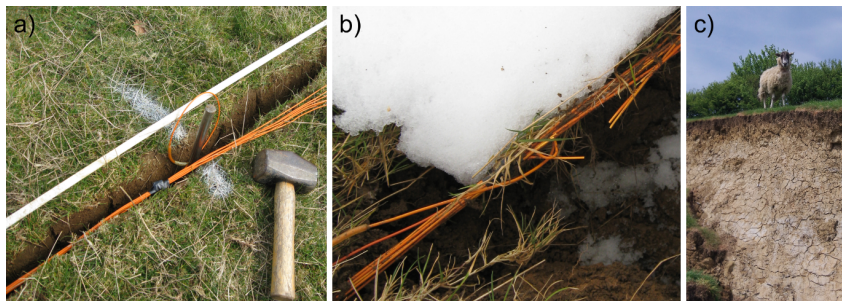

Fig 15.10: a) Burying electrodes and cables at a landslide monitoring site. b) Broken cables. c) Livestock and ground motion, both potential culprits for damage to ERT monitoring installations (BGS © UKRI 2019).

Sources of random error include telluric currents induced by fluctuations in the Earth's magnetic field; self-potential effects from natural ground sources such as ore bodies acting as batteries and streaming potentials due to groundwater motion; and anthropogenic sources of electromagnetic noise such as power lines. They can be reduced in switched DC systems by subtracting slowly varying backgrounds and averaging fast variations, or by filtering in low-frequency AC systems. Signal-to-noise can be maximised by keeping galvanic contact resistances as low as possible, although electrode surface changes due to corrosion and scale formation can cause contact resistances to increase over time in monitoring installations [74], and weather tends to cause higher contact resistances (due to drier, harder ground conditions) with worse data quality in summer months than winter for warmer climates.

Data quality is typically assessed using stacking errors (from repeated measurements made over several cycles during acquisition), repeat errors (from repetitions

of the same survey), and reciprocal errors (by performing the same survey in re-
ciprocal configurations, i.e. with current and potential dipoles exchanged) [75].
Stacking errors are usually smaller than repeat or reciprocal errors since the ground
conditions have less time to change during stacking cycles than during the repeat
period of entire surveys which can take hours due to low excitation frequencies
and large numbers of electrodes. Reciprocal errors tend to be preferred over re-
peat errors since exchanging the dipoles also changes certain factors, such as elec-
trode locations, magnitudes of injected current and received voltage, and degree
of electrode polarization, which helps to identify some types of systematic error.
Per-electrode distributions of errors can be a useful measure to identify problematic
electrodes [76] as can distributions of contact resistances. Poor quality data can be
discarded prior to inversion by filtering out problematic electrodes and setting limits
on error estimates; magnitudes and polarities of apparent resistivity; magnitudes of
geometric factors, return voltages, and contact resistances; and sensitivities to errors
in position.

Once suspect data have been removed, it is often helpful to try to improve error
estimates in individual measurements by constructing an error model [77]. Individ-
ual error estimates can be poor when based on differences between low numbers
of repeat or reciprocal surveys (often only two). Better estimates can be produced
by assuming that the error is a function of transfer resistance, binning the data on a
logarithmic scale, and fitting a low-order polynomial or other simple function to the
averaged data (figure 15.11). Such approaches tend to lead to more robust inverse
models with fewer artefacts, and have recently been extended to cover time-lapse
monitoring data [78] and to account for correlations due to bad electrodes [75].
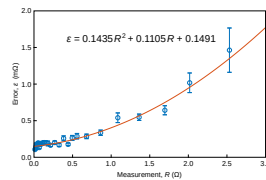

Fig 15.11: Averaged transfer resistance measurements and reciprocal error estimates,
binned on a logarithmic scale, and fitted quadratic error model (BGS © UKRI 2019).

15.12   Data weighting

Apparent resistivities $\varrho = \rho_a$ are transformed ERT *measurements* and do not repre-
sent reconstructed image units. The apparent resistivity transformation is a method

of normalizing the measurement data $\mathbf{b}$ according to a geometric factor k and is essentially a method of re-weighting the data so that the magnitude of the measurements relative to a homogeneous model are all treated equally in the inversion. Without this or a similar correction, the small valued measurements will essentially be ignored because they contribute little to the overall measurement misfit in the reconstructed image. Similar to the log parametrization (see §15.5) the apparent resistivity (15.2) may be formulated as a weighting matrix in the reconstruction, which modifies the data misfit and Jacobian terms

$$\varrho_i = \frac{V_i}{I_i}k \qquad\qquad \varrho = \mathbf{G}_\varrho\,\mathbf{b}$$

$$\mathbf{J}_{\varrho,i,j} = \frac{\partial \varrho_i}{\partial \sigma_j} = \frac{\partial \varrho_i}{\partial \mathbf{b}_i}\frac{\partial \mathbf{b}_i}{\partial \sigma_j} \qquad\qquad \mathbf{J}_\varrho = \mathbf{G}_\varrho\,\mathbf{J}_\sigma \qquad (15.12)$$

for the i-th measurement $\mathbf{b}_i = V_i$ and j-th conductivity element σ_j, where the measured transfer resistance V_i/I_i scaled by the geometric factor k_i. which can be represented as the diagonal measurement normalization matrix $\mathbf{G}_{\varrho,(i,i)} = k_i/I_i$. The conductivity Jacobian $\mathbf{J}_\sigma$ is modified by the same normalization matrix $\mathbf{G}_\varrho$ after applying the chain rule.

The log of apparent resistivity ($\ln \varrho$) is used in ERT reconstructions when the measurements differ from the homogeneous model by orders of magnitude. For example, this range of measurements can occur during a freeze-thaw cycle where liquid ground water (very low resistivity) freezes (very high resistivity). Apparent resistivity can become negative for small magnitude measurements on slightly misplaced electrodes, making log scaling unusable for some datasets [73].

The apparent resistivity conversion results in a right matrix multiplication of $\mathbf{G}_\varrho$ with the conductivity Jacobian $\mathbf{J}_\sigma$ and measurements $\mathbf{b}$. For a time difference Gauss-Newton update, the inverse measurement covariance matrix $\mathbf{W}$ can fulfill the same role as the apparent resistivity measurement transformation

$$\Delta\sigma = (\mathbf{J}_\varrho^\mathsf{T}\mathbf{J}_\varrho + \lambda^2\mathbf{Q})^{-1}\mathbf{J}_\varrho^\mathsf{T}(\Delta\mathbf{b}_\varrho) = (\mathbf{J}_\sigma^\mathsf{T}\mathbf{G}_\varrho^2\mathbf{J}_\sigma + \lambda^2\mathbf{Q})^{-1}\mathbf{J}_\sigma^\mathsf{T}\mathbf{G}_\varrho^2(\Delta\mathbf{b}) \quad (15.13)$$

$$= (\mathbf{J}_\sigma^\mathsf{T}\mathbf{W}\mathbf{J}_\sigma + \lambda^2\mathbf{Q})^{-1}\mathbf{J}_\sigma^\mathsf{T}\mathbf{W}\Delta\mathbf{b} \qquad \text{with } \mathbf{W} = \mathbf{G}_\varrho^2 \qquad (15.14)$$

for change in conductivity $\Delta\sigma$, apparent resistivity Jacobian $\mathbf{J}_\varrho$, regularization $\mathbf{Q}$ with hyperparameter λ, using apparent resistivity time difference measurements $\Delta\mathbf{b}_\varrho$. The inverse measurement covariance $\mathbf{W}$ typically serves to weight the measurements in the reconstruction, often by an estimated noise variance. If an apparent resistivity reconstruction uses a uniform noise estimate $\mathbf{W} = \mathbf{I}$, then using apparent resistivity is exactly equivalent to $\mathbf{W} = \mathbf{G}_\varrho^2$, by which we can see that apparent resistivity is an objective method of applying a data weighting to measurements, possibly modified by available measurement error estimates.

15.13   Available hardware

A sample of available ERT hardware is listed in Table 15.1. The table identifies some key characteristics of commonly available commercial ERT systems currently in use world-wide, including system name and the "source," a company or organization selling and supporting the system. The number of electrodes for some systems are listed as "independent" (indep) and "maximum" (max) numbers of elec-

trodes for systems supporting switching infrastructure between electrode cables (often through external switching boxes): a system supporting 2 cables of at most 256 electrodes would be listed as "256 indep (512 max)." The number of channels "# chan" indicates the number of simultaneous measurements available in the system. Systems supporting switched DC ($\pm$DC) and AC (sinusoidal) stimulus, as well as systems with Induced Polarization (IP) and Self-Potential (SP) measurement capabilities are identified with bullets •. The typical system power requirements and operating frequencies are also listed, where some systems can operate in high or low power modes. There is a remarkable difference in the power requirements of switched DC versus AC systems. For fields where information was not publicly available, question marks "?" have been indicated.

Table 15.1: ERT hardware

System	Source	Electrodes	# chan	$\pm$DC	AC	IP	SP	Power (W)	Freq (Hz)
ALERT	BGS[1]	256 indep (512 max)	10	•		•	•	200	0.5–2
PRIME	BGS	1024 indep	7		•	•		10	0.1–200
GEOMON 4D	GSA[2]	unlimited	> 1?	•		•	•	?[†]	?
GeoTom/ A_ERT	Geolog[3]	100	4		•	•		10	0.5–25
WGDM-9/ WERT-120	Langeo	120	?	•		•	•	7.2k	0.017–1
SuperSting	AGI	224	8	•		•	•	200	0.07–5
ZETA	Zonge Intl.	30 indep (7680 max)	?	?	?	?	?	?	?
Terrameter	ABEM	81 indep (16384 max)	12	•		•	•	250	< 300
IRIS	Syscal	120	10	•		•	•	250/1.2k	0.125–4
4PL	Lippmann	100	1		•	•		10	0.26–30
DAS-1	MPT	64 indep (16384 max)	8	•	•	•	•	250	$\leq 225^*$
IRIS	FullWaver	2/node	1/node	•		•	•	10k	< 50
Flashres	ZZRI	64 indep	61	•				250	0.1–1
Geotection	HGI	∞	180	•			•	960	0.05–5
OhmMapper	Geometrics	?	?	?	?	?	?	?	?
V-fullWaver	II	?	?	?	?	?	?	?	?

BGS: British Geological Survey; GSA: Geological Survey of Austria; MPT: Multi Phase Technologies;
ZZRI: ZZ Resistivity Imaging; II: Iris Instruments; [†] 235 W solar, 25 W fuel cell; [*] 0.016–13.5 DC, ≤ 225 AC;
[1] [79]; [2] [80]; [3] [81]; ?: unpublished
∞: unlimited electrodes (multiplexed in groups of 180);

15.14 Available software

A sample of available ERT software is listed in Table 15.2. The variety of software for ERT reconstructions reflect a mature (if specialized) market with a relatively rich array of commercial offerings. The most common commercial software is likely Res2DInv and Res3DInv (Geotomo), though it is difficult to externally judge uptake by academic and commercial entities. All codes support the point electrode model

(PEM); these have not been indicated in the table.

Table 15.2: ERT software

Software	Author	License	2.5D	3D	IP	CEM
BERT/pyGIMLI	Günther & Rücker	GPLv3+	●	●	●	●
E4D	Johnson/PNNL	BSD		●	●	
R2/R3t	Binley	csf	●	●		
cR2	Binley	csf	●		●	
Res2D/3DInv,	Loke/GeoTomo	$	●	●	●	
ZondRes2dp/3d,	Zonge Intl.	$	●	●	●	
EarthImager2D/3D	AGI USA	$	●	●	●	
ERTLab	MPT	$		●	●	
Aarhus Workbench	HG-AU	$	●		●	
VOXI	Geosoft	$		●	●	
DCIP2D/3D	UBC-GIF	a/$	●	●	●	
DC_2D/3DPro	Kim/KIGAM	a/$	●	●		
ResInvM3D	Pidlisecky	SEG		●		
IP4DI	Karaoulis	BSD	●	●	●	
ELRIS2d	Acka	©	●			
EIDORS	Adler	GPLv2/3	●	●	●	●
SimPEG	Cockett	MIT	●	●	●	
V-fullWaver	Iris Instruments	?	?	?	?	?

$: commercial; ©: source available, copyright retained; a: academic; csf: closed source/freeware; GPLv3+: GPL v3 and Apache v2; SEG: SEG Open Source; PNNL: Pacific Northwest National Laboratory, United States Department of Energy; MPT: Multi Phase Technologies; HG-AU: Hydrogeophysics Group, Aarhus University; UBC-GIF: University of British Columbia Geophysical Inversion Facility; KIGAM: Korea Institute of Geoscience and Mineral Resources

15.15   Discussion

In general, one can observe that the similarities between geophysical ERT and biomedical EIT outweigh the differences. Both EIT and ERT face similar resistivity/conductivity reconstruction issues directly because they are tackling the same mathematical problem. ERT has a long history but many of the major advances in reconstruction and instrumentation have been driven by wider technological advances: the numerical techniques available due to faster, better computational resources, and the availability of improved electronic components. Its long history means that ERT has benefited from a degree of world-wide commercial adoption: a widely recognized electrical tool in geophysical site investigations. EIT has similarly benefited from these enabling technologies, and is perhaps at the cusp of widespread commercial adoption.

There are many examples of parallel research in the two fields of EIT and ERT, but the language used to describe biomedical and geophysical EIT/ERT problems and their solutions differ enough that translational research, or even discovering related research, is challenging. In addition, access controls on the literature limit discoverability because many institutions have either biomedical or geophysical library access to journals but not both. Recent movements toward open access publishing are breaking some of these barriers.

The technical language of EIT and ERT differ in their specifics, including math-

ematical conventions, and the translation to a familiar framework can be challenging. Despite the technical language barriers, there is a richness in exploring geophysical techniques and looking for opportunities to apply these to biomedical problems; opportunities to open new avenues of research or imagine new areas of application.

Acknowledgements

Bibliography

[1] C. Schlumberger, *Étude sur la Prospection Électrique du Sous-sol*. Gauthier-Villars et Cie, 1920.

[2] L. Allaud and M. Martin, *Schlumberger: The History of a Technique*. John Wiley & Sons, 1977.

[3] R. Barker, "Signal contribution sections and their use in resistivity studies," *Geophys. J. Int.*, vol. 59, no. 1, pp. 123–129, 1979.

[4] M. H. Loke and R. Barker, "Rapid least-squares inversion of apparent resistivity pseudosections by a quasi-Newton method," *Geophys. Prospect.*, vol. 44, pp. 131–152, Jan. 1996.

[5] G. E. Archie, "The electrical resistivity log as an aid in determining some reservoir characteristics," *Transactions of the American Institue of Mining, Metallurgical, and Patroleum Engineers*, vol. 146, no. 1, pp. 54–62, 1942.

[6] M. Waxman and L. Smits, "Electrical conductivities in oil-bearing shaly sands," *SPE Journal*, vol. 8, pp. 107–122, June 1968.

[7] P. Glover, "Geophysical properties of the near surface earth: Electrical properties," in *Treatise on Geophysics*, vol. 11, pp. 89–137, Oxford, UK: Elsevier, 2 ed., 2015.

[8] L. Slater, "Near surface electrical characterization of hydraulic conductivity: From petrophysical properties to aquifer geometries — a review," *Surveys in Geophysics*, vol. 28, no. 2-3, pp. 169–197, 2007.

[9] A. Revil, M. Karaoulis, T. Johnson, and A. Kemna, "Review: Some low-frequency electrical methods for subsurface characterization and monitoring in hydrogeology," *Hydrogeology Journal*, vol. 20, no. 4, pp. 617–658, 2012.

[10] M. H. Loke, J. E. Chambers, D. Rucker, O. Kuras, and P. B. Wilkinson, "Recent developments in the direct-current geoelectrical imaging method," *J. Applied Geophys.*, vol. 95, pp. 135–156, Aug. 2013.

[11] A. Perrone, V. Lapenna, and S. Piscitelli, "Electrical resistivity tomography technique for landslide investigation: A review," *Earth-Science Reviews*, vol. 135, pp. 65–82, Aug. 2014.

[12] A. Binley, S. Hubbard, J. Huisman, D. Revil, Robinson, K. Singha, and L. Slater, "The emergence of hydrogeophysics for improved understanding of subsurface processes over multiple scales," *Water Resources Research*, vol. 51, no. 6, pp. 3837–3866, 2015.

[13] A. Malehmir, L. Socco, M. Bastani, C. Krawczyk, A. Pfaffhuber, R. Miller, H. Maurer, R. Frauenfelder, K. Suto, S. Bazin, K. Merz, and T. Dahlin, "Chapter two — near-surface geophysical characterization of areas prone to natural hazards: A review of the current and perspective on the future," *Advances in Geophysics*, vol. 57, pp. 51–146, 2016.

[14] M. Gharibi and L. Bentley, "Resolution of 3-D electrical resistivity images from inversions of 2-D orthogonal lines," *Journal of Environmental and Engineering Geophysics*, vol. 10, no. 4, pp. 339–393, 2005.

[15] J. E. Chambers, D. Gunn, P. B. Wilkinson, P. Meldrum, E. Haslam, S. Holyoake, M. Kirkham, O. Kuras, A. Merritt, and J. Wragg, "4D electrical resistivity tomography monitoring of soil moisture dynamics in an operational railway embankment," *Near Surface Geophysics*, vol. 12, pp. 61–72, Feb. 2014.

[16] M. Karaoulis, P. Tsourlos, J. Kim, and A. Revil, "4D time-lapse ERT inversion: introducing combined time and space constraints," *Near Surface Geophysics*, vol. 12, no. 1, pp. 25–34, 2014.

[17] P. B. Wilkinson, J. Chambers, O. Kuras, P. Meldrum, and D. Gunn, "Long-term time-lapse geoelectrical monitoring," *First Break*, vol. 29, no. 8, pp. 77–84, 2011.

[18] K. Singha, F. Day-Lewis, T. Johnson, and L. Slater, "Advances in interpretation of subsurface processes with time-lapse electrical imaging," *Hydrological Processes*, vol. 29, no. 6, pp. 1549–1576, 2015.

[19] J. Whiteley, J. Chambers, S. Uhlemann, P. B. Wilkinson, and J. Kendall, "Geophysical monitoring of moisture-induced landslides: A review," *Review of Geophysics*, vol. 57, no. 1, pp. 106–145, 2019.

[20] P. B. Wilkinson, M. H. Loke, P. I. Meldrum, J. E. Chambers, O. Kuras, D. A. Gunn, and R. D. Ogilvy, "Practical aspects of applied optimized survey design for electrical resistivity tomography," *Geophys. J. Int.*, vol. 189, pp. 428–440, Apr. 2012.

[21] M. H. Loke, P. B. Wilkinson, J. E. Chambers, S. Uhlemann, and J. P. R. Sorensen, "Optimized arrays for 2-D resistivity survey lines with a large number of electrodes," *Journal of Applied Geophysics*, vol. 112, pp. 136–146, Jan. 2015.

[22] P. B. Wilkinson, S. Uhlemann, P. Meldrum, J. Chambers, S. Carrière, L. Oxby, and M. H. Loke, "Adaptive time-lapse optimized survey design for electrical resistivity tomography monitoring," *Geophys. J. Int.*, vol. 203, no. 1, pp. 755–766, 2015.

[23] F. M. Wagner, T. Günther, C. Schmidt-Hattenberger, and H. Maurer, "Constructive optimization of electrode locations for target-focused resistivity monitoring," *Geophysics*, vol. 80, no. 2, pp. 1MA–Z50, 2015.

[24] S. Uhlemann, P. B. Wilkinson, H. Maurer, F. Wagner, T. Johnson, and J. Chambers, "Optimized survey design for electrical resistivity tomography: combined optimization of measurement configuration and electrode placement," *Geophys. J. Int.*, vol. 214, no. 1, pp. 108–121, 2018.

[25] P. B. Wilkinson, J. Chambers, P. Meldrum, R. Ogilvy, and S. Caunt, "Optimization of array configurations and panel combinations for the detection and imaging of abandoned mineshafts using 3D cross-hole electrical resistivity tomography," *Journal of Environmental & Engineering Geophysics*, vol. 11, no. 3, pp. 161–224, 2006.

[26] O. Kuras, P. B. Wilkinson, P. Meldrum, L. Oxby, S. Uhlemann, J. Chambers, A. Binley, J. Graham, N. Smith, and N. Atherton, "Geoelectrical monitoring of simulated subsurface leakage to support high-hazard nuclear decommissioning at the Sellafield Site, UK," *Science of the Total Environment*, vol. 566–567, pp. 350–359, 2016.

[27] A. Pidlisecky, R. Knight, and E. Haber, "Cone-based electrical resistivity tomography," *Geophysics*, vol. 71, no. 4, pp. G157–G167, 2006.

[28] M. H. Loke, H. Kiflu, P. B. Wilkinson, D. Harro, and S. Kruse, "Optimized arrays for 2D resistivity surveys with combined surface and buried arrays," *Near Surface Geophysics*, vol. 13, no. 5, pp. 505–517, 2015.

[29] G. Tsokas, P. Tsourlos, J. Kim, C. Papazachos, G. Vargemezis, and P. Bogiatzis, "Assessing the condition of the rock mass over the Tunnel of Eupalinus in Samos (Greece) using both conventional geophysical methods and surface to tunnel electrical resistivity tomography," *Archaeological Prospection*, vol. 21, no. 4, pp. 277–291, 2014.

[30] N. Lesparre, A. Boyle, B. Grychtol, J. Cabrerra, J. Marteau, and A. Adler, "Electrical resistivity imaging in transmission between the surface and underground tunnel for fault characterization," *J. Applied Geophys.*, vol. 128, pp. 163–178, May 2016.

[31] P. B. Wilkinson, P. Meldrum, O. Kuras, J. Chambers, S. Holyoake, and R. Ogilvy, "High-resolution electrical resistivity tomography monitoring of a tracer test in a confined aquifer," *J. Applied Geophys.*, vol. 70, no. 4, pp. 268–276, 2010.

[32] S. Wang, T. Kalscheuer, M. Bastani, A. Malehmir, L. Pedersen, T. Dahlin, and N. Meqbel, "Joint inversion of lake-floor electrical resistivity tomography and boat-towed radio-magnetotelluric data illustrated on synthetic data and an application from the äspö Hard Rock Laboratory site, Sweden," *Geophys. J. Int.*, vol. 213, no. 1, pp. 511–533, 2018.

[33] A. Bouchedda, M. Chouteau, A. Binley, and B. Giroux, "2-D joint structural inversion of cross-hole electrical resistance and ground penetrating radar data," *J. Applied Geophys.*, vol. 78, no. 0, pp. 52–67, 2012.

[34] S. Uhlemann, J. E. Chambers, P. B. Wilkinson, H. Maurer, A. Merritt, P. Meldrum, O. Kuras, D. Gunn, A. Smith, and T. Dijkstra, "Four-dimensional imaging of moisture dynamics during landslide reactivation," *Journal of Geophysical Research: Earth Surface*, vol. 122, no. 1, pp. 398–418, 2017.

[35] D. Colombo and D. Rovetta, "Coupling strategies in multiparameter geophysical joint inversion," *Geophys. J. Int.*, vol. 215, no. 2, pp. 1171–1184, 2018.

[36] B. Heincke, M. Jegen, M. Moorkamp, R. Hobbs, and J. Chen, "An adaptive coupling strategy for joint inversions that use petrophysical information as constraints," *J. Applied Geophys.*, vol. 136, pp. 279–297, 2017.

[37] M. Moorkamp, "Integrating electromagnetic data with other geophysical observations for enhanced imaging of the earth: a tutorial and review," *Surveys in Geophysics*, vol. 38, no. 5, pp. 935–962, 2017.

[38] J. Gance, P. Sailhac, and J. Malet, "Corrections of surface fissure effect on apparent resistivity measurements," *Geophys. J. Int.*, vol. 200, no. 2, pp. 1118–1135, 2015.

[39] J. Gance, J. Malet, R. Supper, P. Sailhac, D. Ottowitz, and B. Jochum, "Permanent electrical resistivity measurements for monitoring water circulation in clayey landslides," *J. Applied Geophys.*, vol. 126, pp. 98–115, 2016.

[40] S. Uhlemann, J. Sorensen, A. House, P. B. Wilkinson, C. Roberts, D. Gooddy, A. Binley, and J. E. Chambers, "Integrated time-lapse geoelectrical imaging of wetland hydrological processes," *Water Resources Research*, vol. 52, no. 3, pp. 1607–1625, 2016.

[41] P. B. Wilkinson, J. E. Chambers, S. Uhlemann, P. Meldrum, A. Smith, N. Dixon, and M. H. Loke, "Reconstruction of landslide movements by inversion of 4-D electrical resistivity tomography monitoring data," *Geophysical Research Letters*, vol. 43, pp. 1166–1174, Feb. 2016.

[42] A. Boyle, P. B. Wilkinson, J. E. Chambers, P. I. Meldrum, S. Uhlemann, and A. Adler, "Jointly reconstructing ground motion and resistivity for ERT-based slope stability monitoring," *Geophys. J. Int.*, vol. 212, pp. 1167–1182, Feb. 2018.

[43] M. H. Loke, P. B. Wilkinson, J. E. Chambers, and P. Meldrum, "Rapid inversion of data from 2D resistivity surveys with electrode displacements," *Geophys. Prospect.*, vol. 66, no. 3, pp. 579–594, 2018.

[44] O. Kuras, D. Beamish, P. I. Meldrum, and R. D. Ogilvy, "Fundamentals of the capacitive resistivity technique," *Geophysics*, vol. 71, pp. G135–G152, May 2006.

[45] O. Kuras, P. I. Meldrum, D. Beamish, R. D. Ogilvy, and D. Lala, "Capacitive resistivity imaging with towed arrays," *Journal of Environmental and Engineering Geophysics*, vol. 12, pp. 267–279, Sept. 2007.

[46] M. Neukirch and N. Klitzsch, "Inverting capacitive resistivity (line electrode) measurements with direct current inversion programs," *Vadose Zone Journal*, vol. 9, no. 4, pp. 882–892, 2010.

[47] B. Souffaché, P. Cosenza, S. Flageul, J. Pencolé, S. Seladji, and A. Tabbagh, "Electrostatic multipole for electrical resistivity measurements at the decimetric scale," *J. Applied Geophys.*, vol. 71, no. 1, pp. 6–12, 2010.

[48] J. Murton, O. Kuras, M. Krautblatter, T. Cane, D. Tschofen, S. Uhlemann, S. Schober, and P. Watson, "Monitoring rock freezing and thawing by novel geoelectrical and acoustic techniques," *Journal of Geophysical Research: Earth Surface*, vol. 121, no. 12, pp. 2309–2332, 2016.

[49] A. Binley, "Tools and techniques: Electrical methods," in *Treatise on Geophysics*, vol. 11, pp. 233–259, Oxford, UK: Elsevier, 2 ed., 2015.

[50] T. Dahlin and V. Leroux, "Improvement in time-domain induced polarization data quality with multi-electrode systems by separating current and potential cables," *Near Surface Geophysics*, vol. 10, pp. 545–565, Apr. 2012.

[51] A. Kemna, A. Binley, G. Cassiani, E. Niederleithinger, A. Revil, L. Slater, K. Williams, F. Orozco, F. Haegel, A. Hördt, S. Kruschwitz, V. Leroux, K. Titov, and E. Zimmermann, "An overview of the spectral induced polarization method for near-surface applications," *Near Surface Geophysics*, vol. 10, no. 6, pp. 453–468, 2012.

[52] A. Vinciguerra, M. Aleardi, and P. Costantini, "Full-waveform inversion of complex resistivity IP spectra: Sensitivity analysis and inversion tests using local and global optimization strategies on synthetic datasets," *Near Surface Geophysics*, vol. 17, no. 2, pp. 109–125, 2019.

[53] T. Johnson and J. Thomle, "3-D decoupled inversion of complex conductivity data in the real number domain," *Geophys. J. Int.*, vol. 212, no. 1, pp. 284–296, 2018.

[54] D. LaBrecque and X. Yang, "Difference inversion of ert data: a fast inversion method for 3-d in situ monitoring," *Journal of Environmental and Engineering Geophysics*, vol. 6, no. 2, pp. 83–89, 2001.

[55] K. Hayley, A. Pidlisecky, and L. Bentley, "Simultaneous time-lapse electrical resistivity inversion," *J. Applied Geophys.*, vol. 75, no. 2, pp. 401–411, 2011.

[56] M. H. Loke, T. Dahlin, and D. Rucker, "Smoothness-constrained time-lapse inversion of data from 3D resistivity surveys," *Near Surface Geophysics*, vol. 12, no. 1, pp. 5–24, 2014.

[57] C. Rücker and T. Günther, "The simulation of finite ERT electrodes using the complete electrode model," *Geophysics*, vol. 76, no. 4, pp. F227–F238, 2011.

[58] P. Ridd, "Electric potential due to a ring electrode," vol. 19, no. 3, pp. 464–467, 1994.

[59] T. Ingeman-Nielsen, S. Tomaškovičová, and T. Dahlin, "Effect of electrode shape on grounding resistances — part 1: The focus-one protocol," *Geophysics*, vol. 81, no. 1, pp. 1JF–Z7, 2016.

[60] C. Verdet, Y. Anguy, C. Sirieix, R. Clément, and C. Gaborieau, "On the effect of electrode finiteness in small-scale electrical resistivity imaging," *Geophysics*, vol. 83, no. 6, pp. 1ND–Z38, 2018.

[61] J. Yang, Y. Liu, and X. Wu, "3-D DC resistivity modelling with arbitrary long electrode sources using finite element method on unstructured grids," *Geophys. J. Int.*, vol. 211, no. 2, pp. 1162–1176, 2017.

[62] L. Beff, T. Günther, B. Vandoorne, V. Couvreur, and M. Javraux, "Three-dimensional monitoring of soil water content in a maize field using electrical resistivity tomography," *Hydrology and Earth System Sciences*, vol. 17, no. 2, pp. 595–609, 2013.

[63] F. M. Wagner, P. Bergmann, C. Rücker, B. Wiese, T. Labitzke, C. Schmidt-Hattenberger, and H. Maurer, "Impact and mitigation of borehole related effects in permanent crosshole resistivity imaging: An example from the Ketzin CO_2 storage site," *J. Applied Geophys.*, vol. 123, no. 1, pp. 102–111, 2015.

[64] F. M. Wagner and B. Wiese, "Fully coupled inversion on a multi-physical reservoir model — part II: The Ketzin CO_2 storage reservoir," *International Journal of Greenhouse Gas Control*, vol. 75, no. 1, pp. 273–281, 2018.

[65] C. Rücker, T. Günther, and K. Spitzer, "Three-dimensional modelling and inversion of DC resistivity data incorporating topography - I. Modelling," *Geophys. J. Int.*, vol. 166, no. 2, pp. 495–505, 2006.

[66] A. Dey and H. Morrison, "Resistivity modelling for arbitrarily shaped two-dimensional structures," *Geophys. Prospect.*, vol. 27, no. 1, pp. 106–136, 1979.

[67] Z. Bing and S. Greenhalgh, "Finite element three dimensional direct current resistivity modelling: accuracy and efficiency considerations," *Geophys. J. Int.*, vol. 145, no. 3, pp. 679–688, 2001.

[68] S. Penz, H. Chauris, D. Donno, and C. Mehl, "Resistivity modelling with topography," *Geophys. J. Int.*, vol. 194, no. 3, pp. 1486–1497, 2013.

[69] M. Blome, H. Maurer, and K. Schmidt, "Advances in three-dimensional geoelectric forward solver techniques," *Geophys. J. Int.*, vol. 176, no. 3, pp. 740–752, 2009.

[70] Y. Yuan, J. Qiang, J. Tang, Z. Ren, and Z. Xiao, "2.5D direct-current resistivity forward modelling and inversion by finite-element—infinite-element coupled method," *Geophys. Prospect.*, vol. 64, no. 3, pp. 767–779, 2016.

[71] A. Boyle, *Geophysical applications of electrical impedance tomography*. PhD thesis, Carleton University, Ottawa, Canada, 2016.

[72] D. LaBrecque, M. Miletto, W. Daily, A. Ramirez, and E. Owen, "The effects of noise on Occam's inversion of resistivity tomography data," *Geophysics*, vol. 62, no. 2, pp. 538–548, 1996.

[73] P. B. Wilkinson, J. E. Chambers, M. Lelliot, G. Wealthall, and R. Ogilvy, "Extreme sensitivity of crosshole electrical resistivity tomography measurements to geometric errors," *Geophys. J. Int.*, vol. 173, pp. 49–62, Apr. 2008.

[74] O. Kuras, P. B. Wilkinson, P. I. Meldrum, R. T. Swift, S. S. Uhlemann, J. E. Chambers, F. C. Walsh, J. A. Wharton, and N. Atherton, "Performance assessment of novel electrode materials for long-term ERT monitoring," in *Near Surface Geoscience 2015*, (Turin, Italy), Sept. 2015.

[75] C. Tso, O. Kuras, P. B. Wilkinson, S. Uhlemann, J. E. Chambers, P. Meldrum, J. Graham, E. Sherlock, and A. Binley, "Improved characterisation and modelling of measurement errors in electrical resistivity tomography (ERT) surveys," *J. Applied Geophys.*, vol. 146, no. 1, pp. 103–119, 2017.

[76] J. Deceuster, O. Kaufmann, and M. V. Camp, "Automated identification of changes in electrode contact properties for long-term permanent ERT monitoring experiments," *Geophysics*, vol. 78, no. 2, pp. E79–E94, 2013.

[77] K. Mwakanyamale, L. Slater, A. Binley, and D. Ntarlagiannis, "Lithologic imaging using complex conductivity: Lessons learned from the Hanford 300 area," *Geophysics*, vol. 77, no. 6, pp. E397–E409, 2012.

[78] N. Lesparre, F. Nguyen, A. Kemna, T. Robert, T. Hermans, M. Daoudi, and A. Flores-Orozco, "A new approach for time-lapse data weighting in electrical resistivity tomography," *Geophysics*, vol. 82, no. 6, pp. E325–E333, 2017.

[79] O. Kuras, J. Pritchard, P. Meldrum, J. E. Chambers, P. B. Wilkinson, R. Ogilvy, and G. Wealthall, "Monitoring hyrdaulic processes with automated time-lapse electrical resistivity tomography (ALERT)," *Comptes Rendus Geoscience*, vol. 341, pp. 868–885, Nov. 2009.

[80] R. Supper, D. Ottowitz, B. Jochum, J. Kim, A. Römer, I. Baron, S. Pfeiler, M. Lovisolo, S. Gruber, and F. Vecchiotti, "Geoelectrical monitoring: an innovative method to supplement landslide surveillance and early warning," *Near Surface Geophysics*, vol. 12, pp. 133–150, Feb. 2014.

[81] C. Hilbich, C. Fuss, and C. Hauck, "Automated time-lapse ERT for improved process analysis and monitoring of frozen ground," *Permafrost and Periglacial Processes*, vol. 22, pp. 306–319, Oct. 2011.